



Available online at www.sciencedirect.com

ScienceDirect

[Advances in Space Research 58 \(2016\) 2090–2103](http://Advances in Space Research 58 (2016) 2090–2103)

**ADVANCES IN
SPACE
RESEARCH**
(*a COSPAR publication*)
www.elsevier.com/locate/asr

Comparison of geophysical patterns in the southern hemisphere mid-latitude region

L.A. Da Silva ^{*}, P. Satyamurty, L.R. Alves, V.M. Souza, P.R. Jauer, M.V.D. Silveira, M.S. Echer, R. Hajra, C. Medeiros, J.P. Marchezi, M. Rockenbach, N.R. Rigozo, C.M. Denardini, O. Mendes Jr., A. Dal Lago, L.E.A. Vieira

Instituto Nacional de Pesquisas Espaciais, 12227-010 São José dos Campos, Brazil

Received 1 June 2015; received in revised form 1 April 2016; accepted 5 April 2016

Available online 12 April 2016

Abstract

The effects of high-energy particle precipitation on mesospheric and stratospheric ozone have been investigated during the last decades. However, while these effects have been widely discussed for the auroral region, little is known about the role of the high-energy particle precipitation on the stratospheric composition and thermal structure in the tropical/subtropical region. Here we show that the spatial distribution of both the stratospheric ozone and temperature in the southern hemisphere matches the pattern of the Southern Hemisphere Magnetic Anomaly. We found that during the austral winter and spring, in the subtropical region (below 30° S), the reduction of the stratospheric ozone and temperature occurs systematically in the magnetic anomaly area. The differences between the temperatures inside the magnetic anomaly (60°W) and outside the anomaly (150°E) for 42.5°S from June to November are higher than 2 K. The maximum difference at this latitude is approximately 5.9 K and occurs in October during the austral spring.

© 2016 COSPAR. Published by Elsevier Ltd. All rights reserved.

Keywords: Space climate; Particle precipitation; Radiation belts; Southern Hemisphere Magnetic Anomaly; Stratospheric temperature; Ozone abundance

1. Introduction

Observations of atmospheric and oceanic parameters indicate that the climate is changing on global and regional scales (IPCC, 2013). The changes of the solar energy output (e.g. total and spectral solar irradiance), atmospheric composition, oceanic dynamics, and Earth's surface properties are the main causes of the observed climate change (Hansen et al., 2007). In order to assess the causes of changes on regional scales, it is necessary to distinguish the mechanisms responsible for changes in semi-permanent atmospheric systems such as the Intertropical Convergence Zone (ITCZ), South Atlantic Convergence

Zone (SACZ), Upper Tropospheric Cyclonic Vortex (UTCV), subtropical high-pressure centers, and jet streams.

The region encompassing the South America and adjacent oceans provides a unique scenario to investigate the role of natural drivers on climate change. From the point of view of atmospheric-oceanic sciences, the variability of climatic phenomena such as the El Niño-Southern Hemisphere Oscillation (ENSO) is crucial to understand the evolution of several atmospheric systems. From the point of view of space sciences, the presence of the Southern Hemisphere Magnetic Anomaly (SHMA) provides the opportunity to investigate the coupling between the neutral and ionized components of the atmosphere. However, we noted that the energetic coupling between phenomena observed in the neutral and ionized components of the

* Corresponding author.

E-mail address: ligia.silva@inpe.br (L.A. Da Silva).

atmosphere in the SHMA has not been extensively investigated. For example, we do not know the sensibility of the stratospheric composition and dynamics to the ionization due to bremsstrahlung X-ray emission from precipitating relativistic electrons in the SHMA. Furthermore, we do not know if the variability or the spatial patterns of the stratosphere are related to space weather processes. The main purpose of this paper is to examine if the patterns of stratospheric parameters in the southern hemisphere match the pattern of the geomagnetic field, which is employed here to identify the region affected by particle precipitation in the magnetic anomaly.

Here, we focus on the stratosphere because the evolution of the composition and thermal structure of this layer may play an important role in determining the evolution of the lower atmosphere circulation in the tropics and subtropics (Crook et al., 2008; Vieira et al., 2008; Vieira and Da Silva, 2006). According to Shindell et al. (2004), the analysis of the climate response pattern following large tropical volcanic eruptions suggests a climate response and indicates that the stratosphere temperature and wind anomalies can affect northern hemisphere climate. The effects of the zonal asymmetry in the ozone on climate have been examined in the Northern and Southern Hemispheres. These analyses suggest that changes in the zonal asymmetry of ozone have had important impacts on Southern Hemisphere climate (Crook et al., 2008).

This paper is structured as follows. We present the data sets employed for the analysis in Section 2. We describe and compare the patterns observed in the SHMA in Section 3. Finally, the conclusions are presented in Section 4.

2. Data sets

In order to determine the patterns of the southern hemisphere tropical/subtropical stratosphere we employ observations of the lower stratosphere temperature and ozone abundance. We chose these datasets because they extend for the last 3 decades. Thus, we were able to compute the climatology of the distribution of these parameters.

In order to estimate the monthly lower stratosphere temperature climatology, we used monthly distributions of the lower stratosphere temperature (TLS channels) obtained by Microwave Sounding Units (MSU) (Spencer and Christy, 1993) operating on nine NOAA polar-orbiting platforms from 1979 to 2007. The weighting function for the TLS channel peaks between 15 and 20 km of altitude. We are not aware of any Instrumental problems that could cause the patterns discussed in this manuscript. Furthermore, the similarity between the electronics for different channels is such that it is expected that any effect of the particle fluxes in the magnetic anomaly region would occur in all channels to some degree, which is not observed (Carl Mears, Personal Communication, 2008). In order to analyze the ozone distribution we use TIROS Operational Vertical Sounder (TOVS) system data set compiled by the

International Satellite Cloud Climatology Project (ISCCP) for the period from 1983 to 2007.

Here, we used the geomagnetic field intensity near the surface as a proxy of magnetospheric and ionospheric processes such as the particle precipitation from radiation belts into the upper atmosphere. The lack of continuous and reliable observations of key parameters such as the energy deposition of precipitating high-energy particles in the upper and middle atmosphere do not allow us to establish a direct cause-effect relationship between the space weather processes and the patterns in the stratosphere. Furthermore, we cannot rule out the influence of phenomena related to the electrodynamics of the environment such as lightning, sprites, and terrestrial gamma-ray flashes. Thus, we take into account these caveats when discussing the patterns of the geophysical parameters in the SHMA.

3. Geophysical patterns

3.1. Earth's radiation belts and particle precipitation pattern in the SHMA

The Earth's radiation belts contain high-energy protons, electrons and heavier ions trapped in the Earth's magnetic field (Baker et al., 2004). These particles go through a complex motion which can be decomposed into three components: spiraling motion around the field line; bouncing between mirror points on opposite sides of the magnetic equator; and a drift motion around the Earth, eastward for electrons and westward for protons (see Kivelson and Russell (1995) for a detailed description of trapped particles motion). The drift of both protons and electrons around the Earth takes place on magnetic shells (surfaces of constant values of the McIlwain parameter L, which is the distance in Earth radii at which a dipolar magnetic field line crosses the magnetic equatorial plane). The outer radiation belt extends from approximately three to ten Earth radii above the Earth's Surface, and it is populated mainly by high-energy electrons (0.1–10 MeV). The inner radiation belt extends from approximately 0.1 to 1.5 Earth radii above the Earth's surface. It is populated by protons with energies above 19 MeV and electrons in the range of hundreds of keV. Between the outer and inner radiation belt there is also a slot region devoid of particles.

The electrons fluxes in the outer belt present a strong seasonal dependence. Near the spring, the flux can be a factor of 3 times higher than fall equinoxes, for periods around the summer and winter solstices (Baker and Kanekal, 2008). Also, the radiation belts particle fluxes and dynamic show pronounced variations depending on the 11-year solar cycle, caused by the dominant structures propagating in the inner heliosphere (Baker and Kanekal, 2008). For example, the recurrent high speed solar wind streams are often observed at the declining phase of the solar cycle. If such a structure has southward interplanetary magnetic field, it can cause the enhancement of relativistic electrons flux (Miyoshi et al., 2013). On the other

hand, closer to the solar maxima, coronal mass ejections are the most frequent event. The result of the interaction between coronal mass ejection and the outer radiation belt can lead to its depletion (Alves et al., 2016). However, depending on the solar wind parameters both coronal mass ejection and high speed stream can cause even flux depletion as flux enhancement (Reeves et al., 2003). For extreme solar activity the radiation belts are dramatically compressed, distorted and enhanced (Baker et al., 2004). Looper et al. (2005), for example, verified that a sequence of coronal mass ejection interaction with the inner magnetosphere caused the depletion of the radiation belts at almost all L-values, including the inner belt (sited at $L = 2$) almost completely disappeared after 29-October-2003. Additionally, in the same period, a high electrons flux level was found in the slot region (Baker et al., 2004).

Several magnetospheric processes can lead to particle precipitation in the upper atmosphere. For the radiation belt electrons and ions, the main mechanism of precipitation are Coulomb collisions, charge exchange, and wave-particle interactions (Lyons, 1997). Other processes, related to direct entry of particles into the magnetosphere via the open field lines are precipitation of polar rain, cusp/mantle and energetic solar particles. The relative contribution of each mechanism depends on the interplanetary driver structure and the geomagnetic activity level.

The atmosphere acts as an energy filter as lost particles penetrate deep, with energy being loss by interactions with the neutral atmosphere. Much of the energy deposited by energetic particles creates ion pairs. Generally, the energy deposition through the atmosphere depends on the incident particle type (if electrons or ions) and on its energy (see Fox et al. (2008) for a review of the energy deposition in planetary atmospheres by charged particles). Low energy electrons with around 1 keV energy, can reach the ionosphere penetrating down to around 110 km height, while particles with energies around 10 and 100 keV can reach the middle and upper mesosphere corresponding to 100 and 75 km. On the other hand, protons with 1 MeV, 10 MeV and 100 MeV can reach, respectively, around 100 km, 75 km and deeper affecting the upper stratosphere.

The interaction among electrons with atmospheric neutrals producing bremsstrahlung X-ray which can penetrate deeper in the atmosphere reaching the stratosphere. The electron's origin producing X-ray on the atmosphere are fluxes of solar radiation, galactic cosmic rays, and charged particles precipitating from the magnetosphere. Fig. 1 shows the distribution of the X-ray (3.0–31.5 keV energy range) night-time emission of the upper atmosphere measured by RPS (X-ray spectrometer) device on board of the CORONAS-F satellite (Kuznetsov, 2007). One can note, according to Kuznetsov (2007), the emission of particular regions from SHMA and outer radiation belt in the Northern and Southern hemispheres. The interaction among quasi-trapped particles and molecules of the neutral atmosphere is often observed at lower altitudes near to the mirror points.

In a symmetrical dipole configuration regarding to the Earth's axis, a given particle mirror points can be positioned in such a way that their height related to the Earth's surface is a constant everywhere as it drifts around its shell. However, the present geomagnetic field configuration shows pronounced departures from such a symmetry and, because of the low magnetic field intensity in the southern hemisphere, the particles mirror points on that region, for a given L shell, reach their minimum at heights closer to the Earth's surface. For this reason, in Fig. 1, is remarkable noted the presence of a region over South America and adjacent oceans, i.e. SHMA, where the magnetic field intensity is lower. Additionally, a large electron flux enhancement inside this region at about 700 km is noticeable (see Fig. 2 of Sauvaud et al., 2008). The mirror altitudes over SHMA can reach to ~ 100 km, while in its magnetic conjugate point the mirror altitude is at ~ 600 km in Gledhill (1976). Below the altitude of 100 km, the atmospheric density is great enough to ensure the loss of particles by collision, so that such particles are efficiently removed (Abdu et al., 2005; Nishino et al., 2006; Trivedi et al., 2004). From late 1992 through 1998, Greenspan et al. (1999) used the Low-Energy Composition Analyzer (LICA) instrument on the low altitude polar orbiting SAMPEX spacecraft to survey energetic ions near the magnetic equator. Data obtained from that instrument were used to produce a world map of the LICA SSD count rate for the period of June in 1996. The results showed that the low energy electron flux enhancement measured during storms were maxima at longitudes just west of the SHMA, unevenly distributed in geographic longitude. Also, Horne et al. (2009) find that for the outer radiation belt electrons with energy >1 MeV, the precipitation peaks during the recovery phase and occurs mainly poleward of the SHMA region, while for electrons energy >300 keV the precipitation can be observed everywhere in both hemispheres and it peaks during the main phase of storms.

The two Antarctic rocket campaigns conducted by Sheldon et al. (1988) during the 10 years observed the precipitating electrons triggered by the Siple VLF transmitter. The observations of continuous electron precipitation with sufficient energy to penetrate the atmosphere to an altitude of 60–80 km were found to be consistent with a model of electron transport from the trapped population to the atmosphere. The model requires slow electron pitch angle diffusion of the geomagnetically trapped population and predicts that almost all energetic electron precipitation occurs in the SHMA.

The estimate of the ionization rate due to electron precipitation in middle latitude made by Vampola and Gorney (1983) suggests a peak near 75–90 km altitude due to primary electron energy deposition, whereas the secondary peaks near 35–45 km are due to Bremsstrahlung X-ray penetration. The maximum precipitation rates at SHMA region were estimated to be around 10^{-2} erg/(cm² s) with a spectrum form $j(E) = 1.34 \times 10^5 E^{-2.27}$ (keV). The precipitating particles penetrate deeper in the

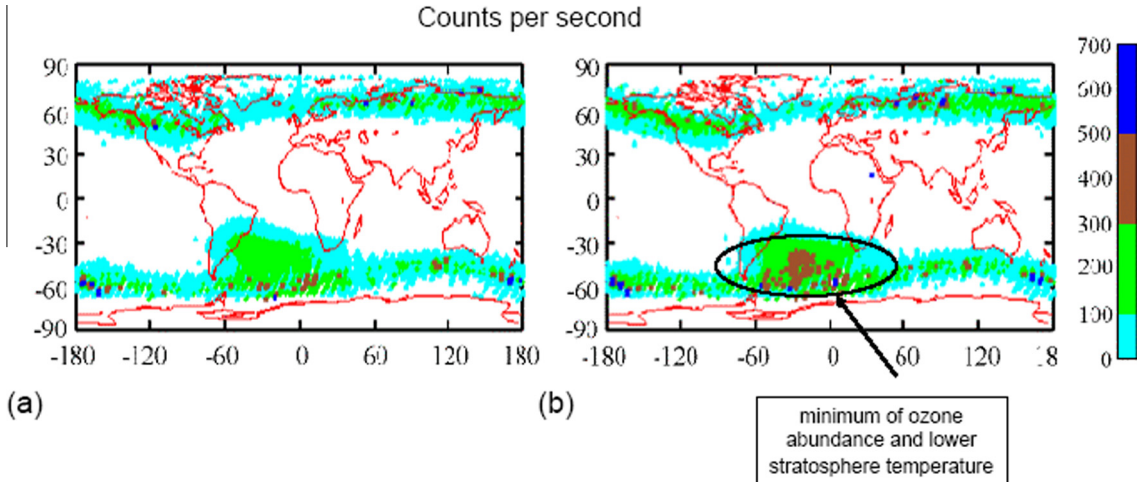


Fig. 1. Distribution of the nighttime X-rays emission of the Earth's atmosphere from 23 September 2002 to 23 March 2003 observed by RPS-1 instrument on board of CORONAS-F satellite. (a) Distribution for the energy interval from 8 to 16 keV. (b) Distribution for the energy interval from 16 to 31 keV. The Southern Hemisphere subtropical region that presents minimum ozone abundance and lower stratosphere temperature is marked in the figure (black line). Adapted from [Kuznetsov \(2007\)](#).

atmosphere in the SHMA region and can lead to more enhanced ionization due to Bremsstrahlung X-ray at low altitudes. From this estimate, the ionization rate associated to the Bremsstrahlung X-ray penetration is about four orders of magnitude smaller than the primary electrons. Balloon-born X-ray measurements have detected energetic electron precipitation effects at stratospheric heights during

intense magnetic disturbances (e.g., [Pinto and Gonzalez, 1986](#); [Pinto and Gonzalez, 1989a,b](#)). [Millan et al. \(2007\)](#) also employing balloon-born X-ray measurements, observed on January 19–20, 2000 an intense bremsstrahlung X-ray emission from relativistic electron precipitation. At the same time, a rapid decrease in the geosynchronous electron flux (>2 MeV) was observed at $L = 4.7$. The

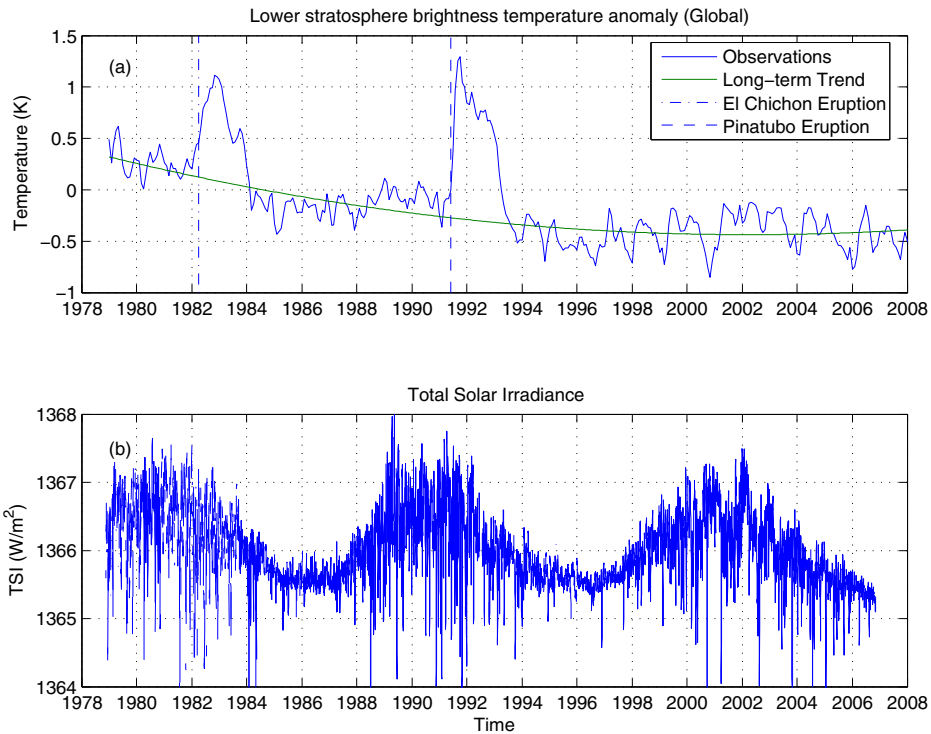


Fig. 2. Global lower stratosphere temperature anomaly. The El Chichon and Pinatubo eruptions are indicated. The green line indicates a long term trend in the temperature (second order polynomial fitting). The Total Solar Irradiance observations (TSI/PMOD Composite) are shown for reference. (For interpretation of the references to color in this figure legend, the reader is referred to the web version of this article.)

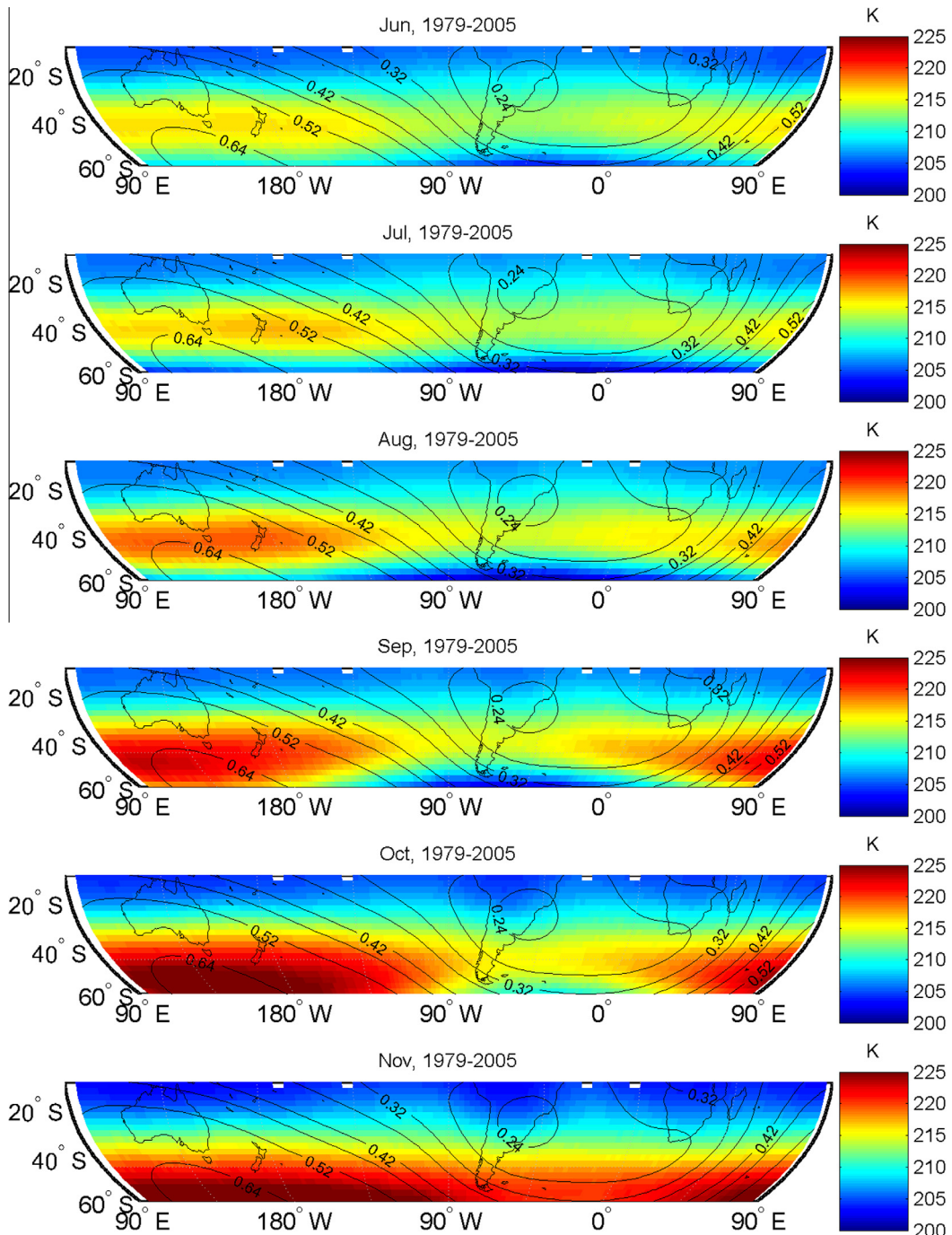


Fig. 3. Southern hemisphere lower stratosphere temperature climatology for June to November. The superimposed black lines show the iso-intensity contours of the geomagnetic field (Gauss) at 10 km for year 1990.

authors suggested that electrons were lost to the atmosphere early in the flux depletion event, during a period of magnetic field stretching in the Earth's magnetotail.

3.2. Stratospheric pattern

Observations indicate that the stratosphere is cooling during the last 3 decades. Fig. 2a shows the anomalies of the lower stratosphere brightness temperature for the

period from 1979 to 2007. A sharp decrease of the temperature is observed from 1979 to approximately 1996. Warming events caused by the eruptions of El Chichon (1982) and Mt Pinatubo (1991) were observed. In addition, the variability of the stratosphere is modulated by the total and spectral solar irradiance and by the ENSO phenomena. Fig. 2b shows for reference the Total Solar Irradiance observations (Fröhlich, 2006). The observations cover near three solar cycles. Lean et al. (2007) modeled the global

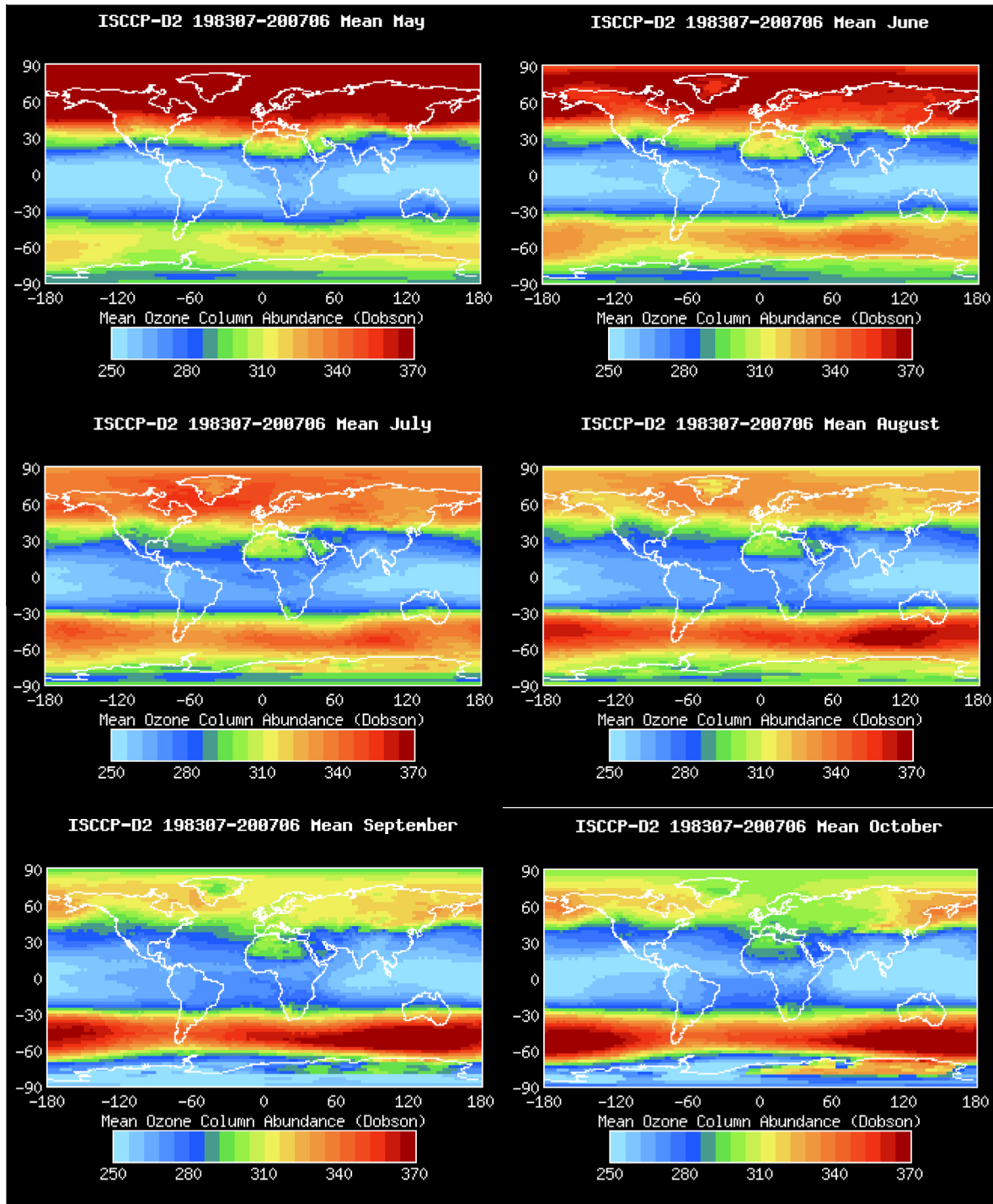


Fig. 4. Mean ozone column abundance distributions from May to October calculated from 1983–2007.

lower stratosphere temperature variability using a multi-parametric fitting. After accounting for the effects of the El Niño-Southern Oscillation (ENSO), volcanic aerosols, and chlorofluorocarbons (CFCs) abundance decrease, the global lower stratosphere temperature approximately in phase with the solar ultraviolet irradiance was noted by [Lean et al. \(2007\)](#). We point out that the climatology of the stratosphere discussed here is affected by the variability of natural and anthropogenic drivers.

[Fig. 3](#) presents the climatology of the lower stratosphere brightness temperature for the Southern Hemisphere. The climatology was computed for June to November using data from 1979 to 2007. The color scale indicates the temperature. Here, we have not removed the trend observed in the global lower stratosphere temperature and the periods of warming events caused by the eruptions of El Chichón (1982) and Mt Pinatubo (1991). Moreover, we have not distinguished periods of high and low solar activity.

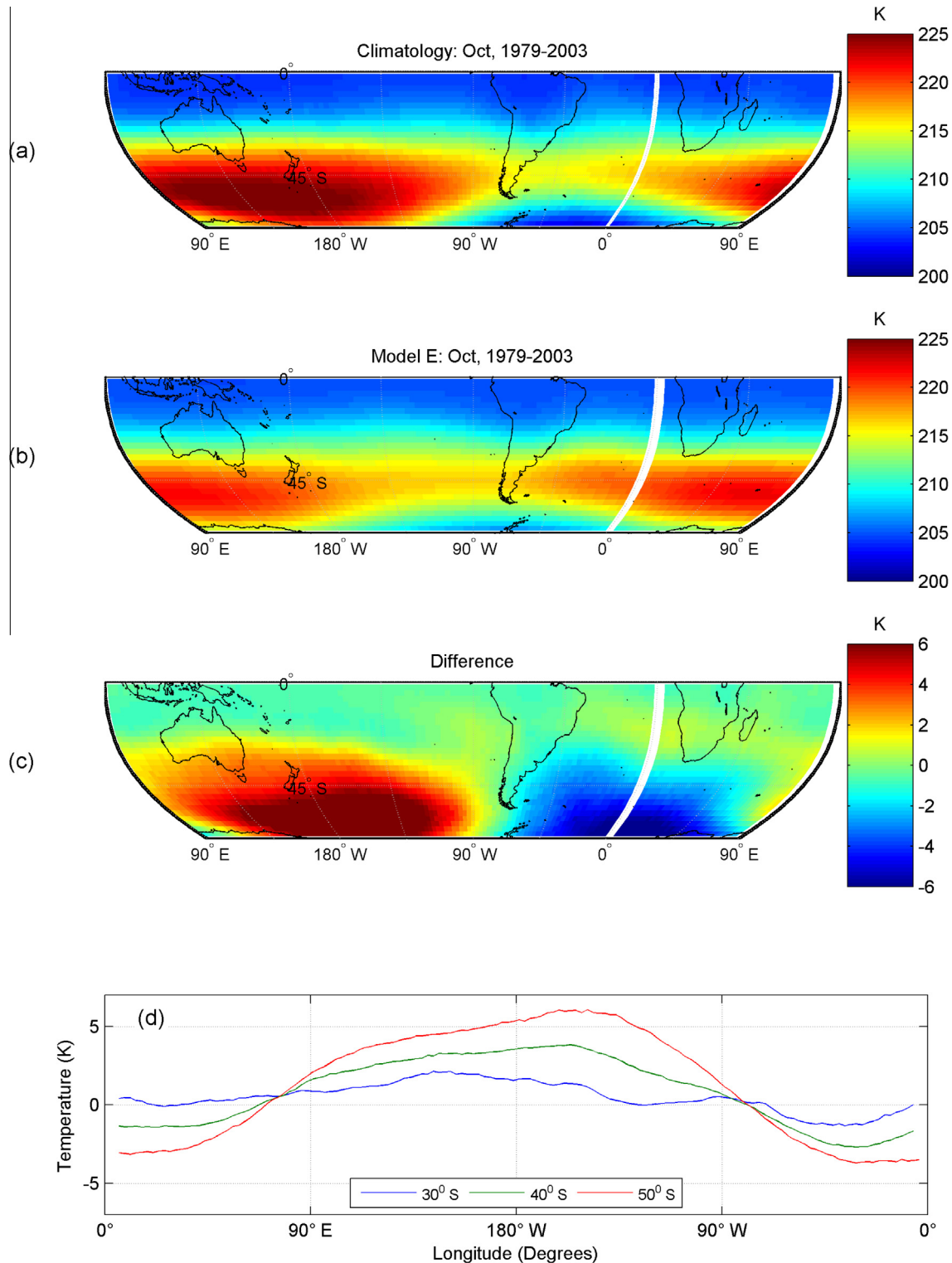


Fig. 5. Comparison between observed (panel a) and modeled (panel b) climatology of the lower stratosphere temperature for October. Panel c presents the difference between the observed and the modeled. Panel d presents the longitudinal profiles at 30°S (blue line), 40°S (green line), and 50°S (red line). (For interpretation of the references to color in this figure legend, the reader is referred to the web version of this article.)

Following (Grytsai et al., 2007b), we focus on these months, as this is generally when both the chemical and dynamical contributions to the zonal ozone asymmetry act, and transport processes associated with the breakdown of the polar vortex are less important.

The atmospheric temperature varies with altitude according to chemical and physical processes taking place. Fig. 4 presents the mean ozone column abundance distribution from May to October calculated from 1983–2007. In the lower stratosphere, air is transported from the

tropics towards the poles by the Brewer–Dobson circulation. The tropical upward branch of the Brewer–Dobson circulation lowers temperatures and ozone concentrations, especially in the lower stratosphere. In the extratropical stratosphere, downwelling causes adiabatic warming and ozone accumulation until the air parcels return to the extratropical troposphere (Deckert and Dameris, 2008). This process contributes to ozone levels in the troposphere. This effect is clearly seen in Fig. 3 during the austral winter. In this region, the upper convective processes in the troposphere affect the tropics so that the temperature has a minimum near the equator and maxima at the summer pole and in winter mid-latitudes. In the upper stratosphere and mesosphere there is a solstice circulation with upward motion in the summer hemisphere, a summer-to-winter transport in the mesosphere and descent near the winter pole.

We note a clear pattern in the lower stratosphere temperature and ozone distributions in the southern hemisphere. Lower temperatures and lower abundance of ozone are observed over South America and the Atlantic Ocean. This pattern is observed from June to November. Here, we refer to this pattern as an asymmetry of the lower stratosphere temperature and ozone distributions. Asymmetries of these parameters are also observed in the Northern Hemisphere. Due to presence of a higher orographic gravity wave sources in the Arctic compared to the Antarctica (Wu and Jiang, 2002), these longitudinal asymmetries in the Northern Hemisphere are not analyzed in this study.

Studies employing zonal harmonic perturbation models of forced planetary wave propagation suggest that the patterns observed are caused by a standing wave. The Antarctica wintertime stratosphere presents a strong near asymmetric flow with fewer orographic gravity wave sources compared to the Arctic (Wu and Jiang, 2002). During the spring, a zonal asymmetry of ozone, temperature and pressure is observed (Grytsai et al., 2007b). The minimum values of the zonal ozone distribution occurs 49.9°W and 6.5°W at 55°S and 75°S, respectively (Grytsai et al., 2007a). Furthermore, an eastward displacement of the zonal minimum from 1979 to 2004 is observed in the longitudinal sector 60°W–0°E while the zonal maximum position is rather stable in the quadrant 90°E–180°E. The asymmetries have been attributed to the Antarctic orography, which could affect the propagation of planetary waves and the zonal distribution of ozone over the Southern polar region, leading to temperature asymmetries. Asymmetries exist in the Northern Hemisphere as well and these asymmetries appear to be strongest in the polar winter season.

The cyclogenesis of mobile anticyclones in the subtropical stratosphere seems to be a key element to understand the patterns observed in the Southern Hemisphere. Quasi-stationary stratospheric anticyclones are observed in both hemispheres (e.g., Aleutian high and Australian high). In addition to quasi-stationary cyclones, mobile anticyclones are also observed. Harvey et al. (2002)

observed that anticyclones during the austral spring are either quasi-stationary or, in general, move eastward. Furthermore, the subtropical region near South America appears to be a region of enhanced anticyclogenesis and the beginning of the pathway for mobile anticyclones. They also observed that anticyclones are often observed to form near South America and then propagate eastward around the Antarctica vortex, past Africa and into the Australian sector. Furthermore, there is frequently more than one anticyclone present during the breakdown of the Antarctic vortex and the merge of anticyclones is often observed. Due to the downward motions, the lower stratosphere inside the anticyclone is warmer and ozone-mixing ratio is higher in comparison with the ambient stratosphere leading directly to a longitudinal asymmetry. In this way, the stratospheric dynamics seems to explain the asymmetry of the lower stratosphere temperature and the ozone distribution.

In order to assess how well state-of-art climate models reproduce the tropical and subtropical patterns of the lower stratosphere in the southern hemisphere, we compare the observations of the lower stratosphere temperature and the output obtained from climate simulations using Model-E of the Goddard Institute for Space Studies (GISS) global climate model. Here we compare with the simulations discussed by Hansen et al. (2007). We focus on the output of the model setup with an ocean–atmosphere coupled scheme and all forcings discussed by Hansen et al. (2007) enabled. The simulations were carried out for the period from 1880 to 2003. In this paper, we employ the averaged distribution of the lower stratosphere temperature computed from 1979 to 2003, which is the overlap period between the observations and the model output. Fig. 5 shows a comparison between the observations (panel a) and the model output (panel b) for October. The difference between the observations and the model output is presented in panel d. The longitudinal difference between the

Table 1

Monthly averaged lower stratosphere temperatures for 42.5°S at Longitudes 60°W and 150°E. The shadowed rows show differences higher than 2 K.

Month	Lower Stratosphere Temperature (K)		Difference (K)
	Longitude: 60°W	Longitude: 150°E	
January	215.29	215.40	0.11
February	215.11	214.64	-0.47
March	214.37	214.77	0.40
April	213.97	215.07	1.10
May	213.37	215.35	1.98
June	213.01	216.33	3.32
July	213.38	216.78	3.40
August	214.19	219.32	5.12
September	214.74	220.39	5.65
October	214.71	220.65	5.94
November	215.44	218.06	2.62
December	215.04	216.20	1.15

observations and the model for 3 fixed latitudes is presented in panel d. We note that the model displays an asymmetry of the distribution of the lower stratosphere temperature. However, the magnitude of the asymmetry is lower than the one presented by the observations. Furthermore, a westward shift of the pattern in relation to the observations is noticeable. Because of the difference of amplitude and the shift between the distributions, a clear dipolar pattern is observed in the distribution presented in panel c. The difference between the South Pacific and the South Atlantic is more than 8 K at 50°S. Similar patterns are also observed during the other months of the austral winter and spring.

3.3. Comparison of the patterns

The superimposed black lines in Fig. 3 show the iso-intensity contours of the geomagnetic field at 10 km in the region of the magnetic anomaly for year 1990. The geomagnetic field was estimated using the International Geomagnetic Reference Field (IGRF) model (Maus et al., 2005). As the purpose of the present analysis is to compare the distribution of the lower stratosphere temperature and the geomagnetic field pattern, the altitude that the magnetic field intensity is computed is not relevant as well as the delimitation of the boundaries of the magnetic anomaly. We note a large reduction of the temperature in

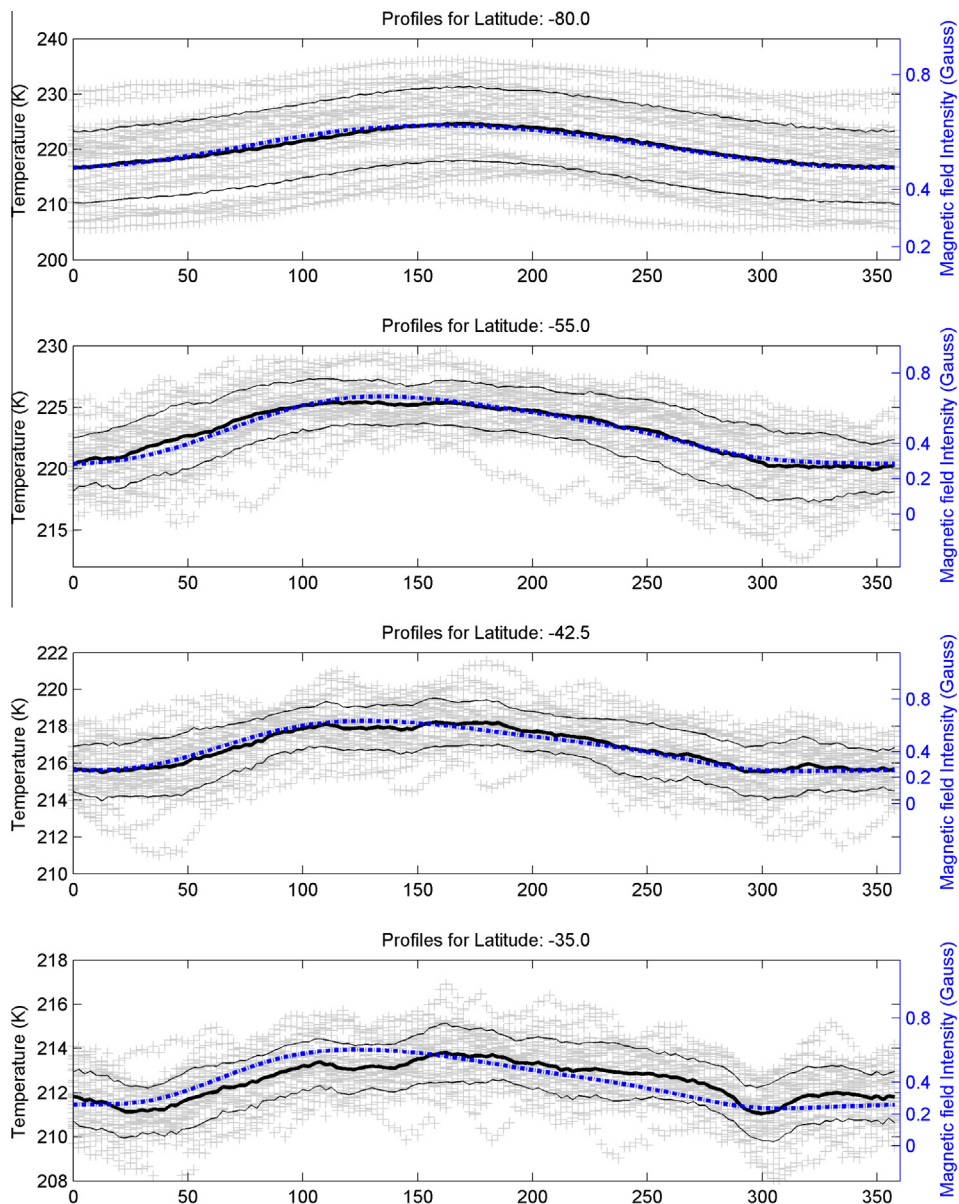


Fig. 6. Longitudinal profiles of the lower stratosphere brightness temperature and the magnetic field intensity for November for the latitudes 80°S, 55°S, 42°S and 35°S. Monthly observations are shown in light gray '+'. The continuous outsized lines show the mean temperature profiles and the tiny lines show the standard deviations. The dotted lines magnetic field intensity (Gauss).

the region of the magnetic anomaly in the belt between 60° S and 30°S during the austral winter and spring, while during the austral summer (not shown here) the reduction in the temperature is not noticeable. This reduction of the temperature coincides quite well with the region, which presents higher electron flux and X-ray emission (see Fig. 1).

The differences between the temperatures inside the magnetic anomaly (60°W) and outside the anomaly (150° E) for 42.5°S from June to November are shown in Table 1. The last column shows the difference between the maximum and minimum region. The differences from June to November are higher than 2 K (shadowed rows). The maximum difference at this latitude is approximately 5.9 K and occurs in October during the austral spring.

Fig. 6 displays the longitudinal profiles of the lower stratosphere brightness temperature and the magnetic field intensity for November. We compute the profiles at the latitudes 80°S, 55°S, 42°S and 35°S. In each panel we show the observations (+), the mean profile (large line), and the standard deviation (tiny line). The dashed line shows the magnetic field profile. It is noticeable that the profiles of the mean temperature and the magnetic field have the

same behavior below 30°S. The maximum temperatures occur near 150°E and the minimum temperatures occur near 60°W.

Table 2 shows the correlation coefficients obtained comparing the mean longitudinal profiles of climatology of lower stratosphere brightness temperature and the magnetic field intensity near surface. It is noticeable the occurrence of a positive correlation below 30°S and a negative correlation above. The positive correlation increases from April to November. The negative correlation is higher during April to September.

Note that although the lower stratosphere temperature, ozone abundance, and the geomagnetic field patterns match in the tropical and subtropical regions of the southern hemisphere, it does not necessarily imply in a direct cause-effect relationship.

One possible mechanism whereby charged particles could have an influence on ozone in the middle to lower stratosphere is the odd nitrogen (NO_y) production (Jackman, 1991; Cubasch and Voss, 2000; Haigh, 2003; Jackman et al., 2005; Randall et al., 2005; Jackman et al., 2015). In this way, in order to observe effects on the ozone the production of NO_y by charged particles should be

Table 2
Correlation coefficients for the Longitudinal profiles of the lower stratosphere temperatures versus magnetic field intensity near surface.

LAT	Jan	Feb	Mar	Apr	May	Jun	Jul	Aug	Sep	Oct	Nov	Dec
0.0	-0.35	-0.17	-0.07	-0.13	-0.40	-0.15	0.10	0.28	0.05	-0.19	-0.46	-0.47
-2.5	-0.36	-0.19	-0.14	-0.16	-0.50	-0.29	-0.05	0.14	-0.06	-0.21	-0.47	-0.50
-5.0	-0.45	-0.30	-0.25	-0.22	-0.60	-0.50	-0.29	-0.08	-0.20	-0.31	-0.51	-0.54
-7.5	-0.52	-0.42	-0.34	-0.30	-0.71	-0.76	-0.58	-0.41	-0.40	-0.44	-0.55	-0.58
-10.0	-0.56	-0.48	-0.41	-0.39	-0.82	-0.92	-0.81	-0.72	-0.63	-0.55	-0.58	-0.58
-12.5	-0.55	-0.50	-0.46	-0.48	-0.89	-0.95	-0.91	-0.89	-0.80	-0.63	-0.58	-0.56
-15.0	-0.51	-0.50	-0.48	-0.55	-0.91	-0.93	-0.93	-0.93	-0.87	-0.66	-0.55	-0.54
-17.5	-0.46	-0.48	-0.50	-0.60	-0.90	-0.89	-0.92	-0.93	-0.88	-0.64	-0.49	-0.49
-20.0	-0.40	-0.45	-0.49	-0.61	-0.88	-0.85	-0.89	-0.90	-0.86	-0.56	-0.39	-0.42
-22.5	-0.32	-0.41	-0.47	-0.56	-0.83	-0.79	-0.85	-0.85	-0.80	-0.38	-0.22	-0.31
-25.0	-0.22	-0.35	-0.41	-0.44	-0.75	-0.69	-0.75	-0.73	-0.60	-0.02	0.04	-0.16
-27.5	-0.10	-0.29	-0.31	-0.17	-0.54	-0.44	-0.52	-0.41	-0.06	0.43	0.35	0.03
-30.0	0.03	-0.22	-0.16	0.16	-0.09	0.13	0.01	0.20	0.54	0.73	0.61	0.25
-32.5	0.16	-0.14	0.06	0.43	0.40	0.64	0.53	0.65	0.79	0.87	0.78	0.45
-35.0	0.26	-0.09	0.26	0.55	0.66	0.83	0.78	0.84	0.88	0.93	0.88	0.61
-37.5	0.29	-0.08	0.34	0.58	0.77	0.88	0.87	0.92	0.90	0.96	0.93	0.71
-40.0	0.16	-0.13	0.26	0.57	0.81	0.91	0.92	0.95	0.89	0.97	0.96	0.75
-42.5	-0.06	-0.21	0.05	0.56	0.81	0.91	0.94	0.96	0.87	0.97	0.98	0.68
-45.0	-0.20	-0.27	-0.16	0.55	0.81	0.91	0.95	0.95	0.83	0.96	0.99	0.45
-47.5	-0.27	-0.29	-0.23	0.55	0.81	0.91	0.95	0.94	0.80	0.95	0.99	0.17
-50.0	-0.31	-0.30	-0.19	0.56	0.82	0.91	0.95	0.93	0.78	0.95	0.98	0.03
-52.5	-0.33	-0.29	-0.11	0.59	0.85	0.92	0.95	0.91	0.77	0.95	0.98	-0.01
-55.0	-0.35	-0.27	-0.00	0.65	0.89	0.93	0.94	0.91	0.77	0.95	0.98	0.01
-57.5	-0.35	-0.25	0.13	0.74	0.93	0.95	0.94	0.91	0.78	0.96	0.98	0.09
-60.0	-0.36	-0.21	0.29	0.83	0.95	0.96	0.93	0.92	0.80	0.97	0.99	0.26
-62.5	-0.36	-0.16	0.47	0.91	0.97	0.97	0.92	0.94	0.82	0.98	0.99	0.52
-65.0	-0.33	-0.08	0.66	0.96	0.97	0.97	0.90	0.95	0.84	0.98	0.99	0.80
-67.5	-0.25	0.03	0.80	0.97	0.96	0.96	0.88	0.96	0.86	0.98	0.99	0.94
-70.0	-0.02	0.21	0.89	0.96	0.95	0.95	0.86	0.96	0.87	0.99	0.99	0.98
-72.5	0.53	0.42	0.93	0.95	0.93	0.94	0.85	0.95	0.88	0.99	0.99	0.98
-75.0	0.88	0.59	0.95	0.94	0.91	0.93	0.83	0.94	0.88	0.99	0.99	0.97
-77.5	0.93	0.69	0.96	0.94	0.89	0.91	0.82	0.94	0.89	0.99	0.99	0.97
-80.0	0.92	0.73	0.97	0.93	0.88	0.91	0.82	0.93	0.89	0.99	0.99	0.97

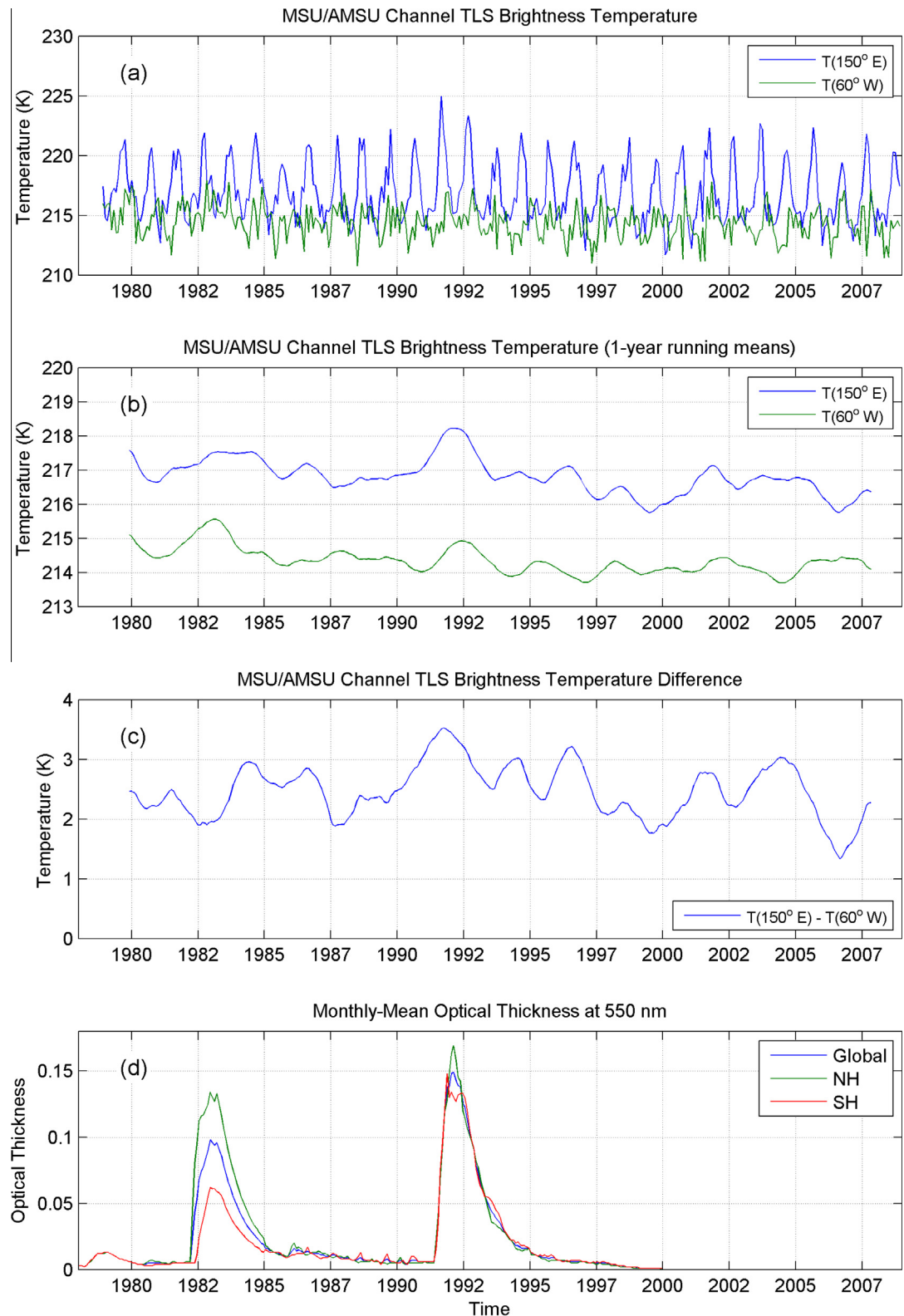


Fig. 7. Comparison of the time evolution of the temperature outside (150°E ; blue line) and inside (60°E ; green line) the magnetic anomaly at 42.5°S (a). Comparison of the filtered signals for the regions outside (blue line) and inside (green line) the SHMA (b) and difference between them (c). Stratospheric aerosol optical thickness at 550 nm (d). (For interpretation of the references to color in this figure legend, the reader is referred to the web version of this article.)

comparable to the ambient levels. In the Southern Hemisphere subtropical latitudes, the NOy levels are approximately 8–12 ppbv at 25 km and approximately 14–16 ppbv at 30 km. During exceptional high activity conditions, the level of ionization from the Bremsstrahlung X-ray radiation could be increased from 0.1 to 1 # cm⁻² s⁻¹, so that it could be comparable to cosmic ray precipitation in this region. Assuming an ionization rate of 1 # cm⁻² s⁻¹ for one day, 1.25 NOy molecules produced per ion pair, and that the destruction and transport of NOy is negligible in this time scale, then 1.1×10^5 NOy molecules are formed, which is about 0.0001 ppbv at 25 km and about 0.0003 ppbv at 30 km. Comparing these values with the ambient levels, we can conclude that the particle precipitation would not lead to the patterns observed.

The results clearly indicate a seasonal variation of the lower stratosphere temperature. In order to isolate the seasonal variation, we present in Fig. 7a a comparison of the time evolution of the temperature outside (150°E; blue line) and inside (60°E; green line) the magnetic anomaly at 42.5° S. While a large seasonal variability is observed outside the magnetic anomaly, a small variability is observed inside. Furthermore, a modulation of the signal is observed outside the anomaly. The variability of the two regions seems to be not related as indicated by the low correlation coefficient ($R_c = 0.07$).

In order to remove the seasonal variability of the time series, we apply a 1-year running mean filter. Fig. 7b presents a comparison of the filtered signals for the regions outside (blue line) and inside (green line) the SHMA, while Fig. 7c presents the difference between them. A difference of approximately 2.5 K is observed after removing the seasonal variability. At this time scale, the correlation coefficient is approximately 0.56. For reference, the stratospheric aerosol optical thickness at 550 nm Sato et al. (1993) is presented in Fig. 7d. The blue curve displays the global monthly mean values, while the green and red lines indicated north hemisphere and south hemisphere monthly-mean values, respectively. The two large peaks were caused by the eruptions of El Chichon (1982) and Mt Pinatubo (1991) and they are related to periods of global warming events in the stratosphere as mentioned above. The warming during the eruption events is observed in both time series. The maximum value of the temperature outside the anomaly is observed after the Mt Pinatubo events while the maximum value inside the anomaly is observed during the El Chichon event. The maximum difference (~3.5 K) between the regions inside and outside the anomaly is observed after the Mt Pinatubo event. During the El Chichon eruption, the difference is below the average (~2 K). The minimum of the temperature difference is observed in 2006 (~1.4 K).

4. Concluding remarks

While the effects of high-energy particle precipitation on ozone distribution in the auroral region have been

investigated during the last decades, little is known about the role of the high-energy particle precipitation on the stratospheric composition and thermal structure in the tropical/subtropical region.

During the austral winter and spring, in the subtropical region (below 30°S), the reduction of the lower stratosphere temperature occurs systematically in the magnetic anomaly area. Precipitating protons and electrons from the radiation belts deposit energy at different heights depending on the particle energy. Most of the energy deposited by electrons ionized the Mesosphere. The secondary ionization peak due to penetrating Bremsstrahlung X-rays occurs in the stratosphere. Although it is not possible to compare directly the distributions of nighttime X-rays emission (Fig. 1), the distributions of lower stratosphere temperature (Fig. 3), and total column ozone abundance (Fig. 4) because of the different observation period, a visual inspection and statistical analysis (Tables 1 and 2) reveals a good correlation between the region with higher particle precipitation (higher emission of X-rays) and the subtropical region that presents minimum temperatures in the lower stratosphere and ozone abundance. One difficulty with this hypothesis is that the production of odd Nitrogen is too low to explain a direct effect of particle precipitation on the ozone abundance in the SHMA.

The formation of mobile anticyclones near the South America, in the magnetic anomaly region, and its propagation eastward suggests that the reduction of the low stratosphere temperature and ozone abundance could result from a net effect of the energy deposition of precipitating particles. Several processes related to the electrodynamics of the environment such as lightning, sprites, and terrestrial gamma-ray flashes (TGFs) could be involved. Furthermore, effects of the Antarctic orography on the propagation of planetary waves seem to contribute to the observed asymmetry.

From the data set analyzed presented here, it is not possible to distinguish if the asymmetry of the stratospheric parameters is related to the precipitation of particles. In addition, it is also not possible to distinguish if the effects of particle precipitation occur in the lower/middle stratosphere due to penetrating Bremsstrahlung X-rays, or, in the lower mesosphere/upper stratosphere propagating downward through the downward branch of the Brewer–Dobson circulation. More sophisticated analysis of the ozone variability in the magnetic anomaly region during periods of different geomagnetic activity levels is necessary to verify the role of particle precipitation in the atmospheric composition and dynamics in the region of the magnetic anomaly.

Acknowledgements

MSU/AMSU data are produced by Remote Sensing Systems and sponsored by the NOAA Climate and Global Change Program. Data are available at www.remss.com. The ISCCP D2 data/images were obtained from the

International Satellite Cloud Climatology Project web site <http://isccp.giss.nasa.gov> maintained by the ISCCP research group at the NASA Goddard Institute for Space Studies, New York, NY. on January 2010. The GISS Model E output is available at the web site <http://data.giss.nasa.gov/modelE/> on February 2010. The authors would like also to thank to Carl Mears for the comments and discussions about the MSU data set. Ligia Alves da Silva is grateful for financial support from the Brazilian National Council for Scientific and Technological Development (CNPq/MCTI: PCI-DA: 313698/2014-7 and PCI-DA: 312743/2015-7). Clezio Marcos Denardini thanks CNPq/MCTI (Grant 03121/2014-9) and FAPESP (Grant 2012/08445-9). Marlos Rockenbach also thanks CNPq/MCTI (Grants 300300/2012-3 and 301495/2015-7). Alisson Dal Lago thanks CNPq/MCTI (Grant 304209/2014-7).

References

- Abdu, M.A., Batista, I.S., Carrasco, A.J., Brum, C.G.M., 2005. South atlantic magnetic anomaly ionization: a review and a new focus on electrodynamic effects in the equatorial ionosphere. *J. Atmos. Solar Terr. Phys.* 67, 1643–1657.
- Alves, L.R., Da Silva, L.A., Souza, V.M., Sibeck, D.G., Jauer, P.R., Vieira, L.E.A., Walsh, B.M., Silveira, M.V.D., Marchesi, J.P., Rockenbach, M., Dal Lago, A., Mendes, M., Tsurutani, B.T., Koga, D., Kanekal, S.G., Baker, D.N., Wygant, J.R., Kletzing, C.A., 2016. Outer radiation belt dropout dynamics following the arrival of two interplanetary coronal mass ejections. *Geophys. Res. Lett.* 43. <http://dx.doi.org/10.1002/2015GL067066>.
- Baker, D.N., Kanekal, S.G., Li, X., Monk, S.P., Goldstein, J., Burch, J.L., 2004. An extreme distortion of the van allen belt arising from the 'hallowe'en' solar storm in 2003. *Nature* 432 (7019), 878–881.
- Baker, D.N., Kanekal, S.G., 2008. Solar cycle changes, geomagnetic variations, and energetic particle properties in the inner magnetosphere. *JASTP* 70 (2–4), 195–206.
- Crook, J.A., Gillett, N.P., Keeley, S.P.E., 2008. Sensitivity of southern hemisphere climate to zonal asymmetry in ozone. *Geophys. Res. Lett.* 35 (7), 1–5.
- Cubasch, U., Voss, R., 2000. The Influence of Total Solar Irradiance on Climate. *Space Science Reviews*, 94. Kluwer Academic Publishers, Printed in the Netherlands, 185–198.
- Deckert, R., Dameris, M., 2008. Atmospheric science: from ocean to stratosphere. *Science* 322 (5898), 53–55.
- Fox, J.L., Galand, M.I., Johnson, R.E., 2008. Energy deposition in planetary atmospheres by charged particles and solar photons. *J. Space Sci. Revi.* 139, 3–62, <http://link.springer.com/chapter/10.1007/978-0-387-87825-6_2>. Springer New York.
- Fröhlich, C., 2006. Solar irradiance variability since 1978. *Space Sci. Rev.* 125 (1), 53–65.
- Gledhill, J., 1976. Aeronomic effects of the south atlantic anomaly. *Rev. Geophys.* 14 (2), 173–187.
- Greenspan, M.E., Mason, G.M., Mazur, J.E., 1999. Low-altitude equatorial ions: a new look with SAMPEX. *J. Geophys. Res.* 104, 19911–19922.
- Grytsai, A.V., Evtushevsky, A., Milinevsky, G., Agapitov, A., 2007a. Longitudinal position of the quasi-stationary wave extremes over the antarctic region from the toms total ozone. *Int. J. Remote Sens.* 28 (6), 1391–1396.
- Grytsai, A.V., Evtushevsky, O.M., Agapitov, O.V., Klekociuk, A.R., Milinevsky, G.P., 2007b. Structure and long-term change in the zonal asymmetry in antarctic total ozone during spring. *Ann. Geophys.* 25 (2), 361–374.
- Haigh, J.D., 2003. The effects of solar variability on the earth's climate. *Philos. Trans. R. Soc.* 361, 95–111.
- Hansen, J., Sato, M., Ruedy, R., Kharecha, P., Lacis, A., Miller, R.L., Nazarenko, L., Lo, K., Schmidt, G.A., Russell, G., Aleinov, I., Bauer, S., Baum, E., Cairns, B., Canuto, V., Chandler, M., Cheng, Y., Cohen, A., Del Genio, A., Faluvegi, G., Fleming, E., Friend, A., Hall, T., Jackman, C., Jonas, J., Kelley, M., Kiang, N.Y., Koch, D., Labow, G., Lerner, J., Menon, S., Novakov, T., Oinas, V., Perlitz, J.P., Perlitz, J., Rind, D., Romanou, A., Schmunk, R., Shindell, D., Stone, P., Sun, S., Streets, D., Tausnev, N., Thresher, D., Unger, N., Yao, M., Zhang, S., 2007. Climate simulations for 1880–2003 with Giss model E. *Clim. Dyn.* 29 (7), 661–696.
- Harvey, V.L., Pierce, R.B., Fairlie, T.D., Hitchman, M.H., 2002. A climatology of stratospheric polar vortices and anticyclones. *J. Geophys. Res.* 107 (NO. D20), 4442. <http://dx.doi.org/10.1029/2001JD001471>.
- Horne, R.B., Lam, M.M., Green, J.C., 2009. Energetic electron precipitation from the outer radiation belt during geomagnetic storms. *Geophys. Res. Lett.* 36, L19104. <http://dx.doi.org/10.1029/2009GL040236>.
- IPCC, 2013. Climate change 2013: the physical science basis. In: Stocker, T.F., Qin, D., Plattner, G.-K., Tignor, M., Allen, S.K., Boschung, J., Nauels, A., Xia, Y., Bex, V., Midgley, P.M. (Eds.), Contribution of Working Group I to the Fifth Assessment Report of the Intergovernmental Panel on Climate Change. Cambridge University Press, Cambridge, United Kingdom and New York, NY, USA, p. 1535. <http://dx.doi.org/10.1017/CBO9781107415324>.
- Jackman, C.H., 1991. Effects of energetic particles on minor constituents of the middle atmosphere. *J. Geomag. Geoelectr.* 43, 637–646.
- Jackman, C.H., De Land, M.T., Labow, G.J., Fleming, E.L., Weisenstein, D., Ko, M.K.W., Sinnhuber, M., Russell, J.M., 2005. Neutral Atmospheric Influences of the Solar Proton Events in October–November 2003. *J. Geophys. Res.–Space Phys.* 110 (A9), A09S27. <http://dx.doi.org/10.1029/2004JA010888>.
- Jackman, C.H., Marsh, D.R., Kinnison, D.E., Mertens, C.J., Fleming, E. L., 2015. Atmospheric changes caused by galactic cosmic rays over the period 1960–2010. *Atmos. Chem. Phys. Discuss.* 15, 33931–33966. <http://dx.doi.org/10.5194/acpd-15-33931-2015>.
- Kivelson, M.G., Russell, C.T., 1995. *Introduction to Space Physics*. Cambridge University Press, Cambridge.
- Kuznetsov, V.D., 2007. From the geophysical to heliophysical year: the results of the coronas-F project. *Russ. J. Earth Sci.* 9, ES3004. <http://dx.doi.org/10.2205/2007ES000276>.
- Lean, J.L., Rind, D., Lonergan, P., 2007. Patterns of Climate Response to Solar and Anthropogenic Influences in the Recent Past, *Eos Trans. In: AGU – Fall Meet. Suppl.*, 88(52), Abstract GC41B-01.
- Looper, M.D., Blake, J.B., Mewaldt, R.A., 2005. Response of the inner radiation belt to the violent sun-earth connection events of October/ November 2003. *Geophys. Res. Lett.* 32 (3), 1–4.
- Lyons, L.R., 1997. Magnetospheric processes leading to precipitation. *Space Sci. Rev.* 80 (1), 109–132.
- Maus, S., Macmillan, S., Chernova, T., Choi, S., Dater, D., Golovkov, V., Lesur, V., Lowes, F., Luhr, H., Mai, W., McLean, S., Olsen, N., Rother, M., Sabaka, T., Thomson, A., Zvereva, T., 2005. The 10th-generation international geomagnetic reference field. *Geophys. J. Int.* 161 (3), 561–565.
- Millan, R.M., Lin, R.P., Smith, D.M., McCarthy, M.P., 2007. Observation of relativistic electron flux during a rapid decrease of trapped relativistic electron flux. *Geophys. Res. Lett.* 34, L10101. <http://dx.doi.org/10.1029/2006GL028653>.
- Miyoshi, Y., Kataoka, R., Kasahara, Y., Kumamoto, A., Nagai, T., Thomsen, M.F., 2013. High-speed solar wind with southward interplanetary magnetic field causes relativistic electron flux enhancement of the outer radiation belt via enhanced condition of whistler waves. *Geophys. Res. Lett.* 40, 4520–4525. <http://dx.doi.org/10.1002/grl.50916>.
- Nishino, M., Makita, K., Yumoto, K., Miyoshi, Y., Schuch, N.J., Abdu, M.A., 2006. Energetic particle precipitation in the brazilian geomag-

- netic anomaly during the “Bastille Day Storm” of July 2000. *Earth Planets Space* 58 (5), 607–616.
- Pinto, O., Gonzalez, W., 1986. X-ray measurements at the south atlantic magnetic anomaly. *J. Geophys. Res.* 91 (A6), 7072–7078.
- Pinto, O., Gonzalez, W.D., 1989a. X-ray measurements in the atmospheric-environment of brazil. *Nucl. Instrum. Methods Phys. Res. Sect. A* 280 (2–3), 499–502.
- Pinto, O., Gonzalez, W.D., 1989b. Energetic electron-precipitation at the South-Atlantic-magnetic-anomaly – a review. *J. Atmos. Terr. Phys.* 51 (5), 351–365.
- Randall, C.E., Harvey, V.L., Manney, G.L., Orsolini, Y., Codrescu, M., Sioris, C., Brohede, S., Haley, C.S., Gordley, L.L., Zawodny, J.M., Russell, J.M., 2005. Stratospheric effects of energetic particle precipitation in 2003–2004. *Geophys. Res. Lett.* 32 (5). <http://dx.doi.org/10.1029/2004GL022003>.
- Reeves, G.D., McAdams, K.L., Friedel, R.H.W., O'Brien, T.P., 2003. Acceleration and loss of relativistic electrons during geomagnetic storms. *Geophys. Res. Lett.* 30, 1529. <http://dx.doi.org/10.1029/2002GL016513>, 10.
- Sato, M., Hansen, J.E., McCormick, M.P., Pollack, J.B., 1993. Stratospheric aerosol optical depths, 1850–1990. *J. Geophys. Res.* 98, 22987–22994. <http://dx.doi.org/10.1029/93JD02553>.
- Sauvaud, J., Maggiolo, R., Jacquay, C., Parrot, M., Berthelier, J.J., Gamble, R.J., Rodger, C.J., 2008. Radiation belt electron precipitation due to VLF transmitters: satellite observations. *Geophys. Res. Lett.* 35 (9), 1–5.
- Sheldon, W.R., Benbrook, J.R., Bering, E.A., 1988. Rocket investigations of electron precipitation and VLF waves in the Antarctic upper atmosphere. *Rev. Geophys.* 26 (3), 519–533. <http://dx.doi.org/10.1029/RG026i003p00519>.
- Shindell, D.T., Schmidt, G.A., Mann, M.E., Faluvegi, G., 2004. Dynamic winter climate response to large tropical volcanic eruptions since 1600. *J. Geophys. Res.* 109.
- Spencer, R.W., Christy, J.R., 1993. Precision lower stratospheric temperature monitoring with the msu - technique, validation, and results 1979–1991. *J. Clim.* 6 (6), 1194–1204.
- Trivedi, N.B., Trivedi, N.B., Abdu, M.A., Pathan, B.M., Dutra, S.L.G., Schuch, N.J., Santos, J.C., Barreto, L.M., 2004. Amplitude enhancement of Sc(H) events in the South Atlantic anomaly region. *J. Atmos. Solar Terr. Phys.* 67 (17–18), 1751–1760, December 2005.
- Vampola, A., Gorney, D., 1983. Electron energy deposition in the middle atmosphere. *J. Geophys. Res.* 88 (A8), 6267–6274.
- Vieira, L.E.A., da Silva, L.A., 2006. Geomagnetic modulation of clouds effects in the Southern Hemisphere Magnetic Anomaly through lower atmosphere cosmic ray effects. *Geophys. Res. Lett.* 33, L14802.
- Vieira, L.E.A., da Silva, L.A., Guarneri, F.L., 2008. Are changes of the geomagnetic field intensity related to changes of the tropical pacific sea-level pressure during the last 50 years? *J. Geophys. Res.* 113, A08226.
- Wu, D.L., Jiang, J.H., 2002. Mls observations of atmospheric gravity waves over Antarctica. *J. Geophys. Res.* 107 (D24). ACL 14-11-ACL 14-16.